Bull. Mater. Sci. (2022) 45:227
https://doi.org/10.1007/s12034-022-02804-3

Structural, morphological, optical and electrical properties of Ni-doped SnO_2 thin films by pneumatic spray pyrolysis method

SABRINA ROGUAI[1,2,*] and ABDELKADER DJELLOUL[1,2]

[1]LASPI2A Laboratory of Structures, Properties and Interatomic Interactions, Abbes Laghrour University, Khenchela 40000, Algeria

[2]Science of Matter, Abbes Laghrour University, Khenchela 40000, Algeria

*Author for correspondence (rog.sabrina@yahoo.fr)

MS received 11 April 2022; accepted 12 July 2022

Abstract. In this study, we used a pneumatic spray pyrolysis technique at 450°C to deposit $Sn_{1-x}Ni_xO_2$ thin films ($0.0 \leq x \leq 0.10$) on glass substrates. The influence of doping content on the films structural, morphological, optical and electrical properties was investigated. Structural characterization by X-ray diffraction indicated that the rutile phase of SnO_2 is present in all thin films, and crystallite sizes are estimated to be in the range of 27–47 nm. Furthermore, structural and microstructural analyses revealed that at $x = 0.05$, there is a solubility limit for (Ni/Sn) in the SnO_2 matrix. The optical bandgap energy increases from 3.83 to 4.01 eV as the dopant content increases according to the Burstein-Moss effect. Resistivity is affected by doping and the thickness of thin films. The figure-of-merit calculated for all samples showed significant differences in the Ni–SnO_2 thin films. There was a difference between the doped thin films depending on the thickness. The lowest resistivity of 1.32×10^{-2} Ω cm and the maximum conductivity of 75 Ω^{-1} cm^{-1} was found at a Ni content of 2%. Seebeck coefficient of all the thin films developed had n-type conductivity, and the values of 76, 71, 133 and 69 μ V/K for Ni-doped SnO_2 thin films at 0, 2, 5 and 10 at.%, respectively, were found to improve the thermoelectric properties of SnO_2 by Ni doping.

Keywords. Ni-doped SnO_2 thin films; pneumatic spray pyrolysis; Seebeck coefficient; optical properties.

1. Introduction

As a result of their unique structural (suitable textured morphology), electrical (relatively low resistivity, on the order of 10^{-15} Ω sq^{-1}), and optical (high optical transmittance) characteristics, transparent semiconductor oxide (TCO) thin films have been the subject of intense research for several years [1,2]. These materials are very important from a technological point of view, and their applications are extremely diverse; they are found in sectors such as electronics [3], silicon solar cells [4], optoelectronics [1] and photovoltaic conversion [5]. Tin oxide is one of these chemicals (SnO_2).

Tin dioxide is the most common tin ore. It crystallizes in a rutile-like structure in its native state (as casseterite). It has the following lattice parameters: $a = b = 4.74$, $c = 3.19$ [6]. SnO_2 is a wide bandgap energy semiconductor. It is transparent in the visible light. The gap of tin oxide in thin films varies between 3.6 and 4.2 eV. Its variances are due to the procedures that were used for its development. On the other hand, this bandgap energy is sufficiently large not to allow activation of the carriers at high temperatures, a process that strongly decreases the Seebeck coefficient. In this regard, inexpensive, environmentally friendly, non-toxic, and high-performance thermoelectric materials are extremely requested, such as SnSe [7], $SnSe_2$ [8], and SnTe [9].

The tin oxide bandgap is of direct type, the valence band and conduction band extrema are on the same axis. Electrons transitions from the valence band to the conduction band are vertical, and free electron concentrations in tin oxide range from 10^{19} to 10^{20} cm^{-3}. It can be doped to improve its electrical properties. Antimony (Sb), niobium (Nb), indium (In), fluorine (F) or chlorine (Cl) doping can improve the conduction characteristics of tin oxide [10].

SnO_2 is an n-type semiconductor [11]. The electrical conductivity of this material is mainly due to the non-stoichiometry of this material deposited in thin films, which causes oxygen vacancies to appear during the synthesis of these thin films. These gaps increase the conduction because they create levels under the conduction band that ionize. Tin oxide has a first ionization energy of 30 meV below the conduction band. Interstitial atoms also participate in the conduction of undoped TCO. This type of doping is done by replacing metal or oxygen atoms. Such doping depends on the size of the dopant and its solubility in the transparent conducting oxide lattice [12]. The doping of tin oxide is possible with elements such as fluorine (F), antimony (Sb),

Published online: 16 November 2022

niobium (Nb), tantalum (Ta), as well as with some metals such as copper (Cu), iron (Fe), cobalt (Co) and nickel (Ni). As for zinc oxide, it is generally doped with aluminium (Al) but also with gallium (Ga) and indium (In) [10,13,14].

Indeed, this type of material provides a good compromise between transparency in the visible and good electrical conductivity, but it is also known for its reflectivity in the infrared and its applications to gas sensors [7], smart window technologies [3]. SnO_2-based thin films are also used in the manufacture of smart windows, thanks to the possibility of modulating the transmitted light.

In order to optimize the light entering the SnO_2 thin films, the light absorption should be reduced, either via a low carrier concentration, which is one of the main mechanisms of free carrier absorption (FCA), or via a reduction of the layer thickness. On the other hand, reducing the mobility of the carriers in the TCO layer would decrease the recovery efficiency of the current generated in the cell, as would a thinner and therefore more resistive layer [3]. Among these nickel-doping elements, Ni^{2+} ions are inserted into the SnO_2 lattice to enhance the carrier concentration of the samples and cause disequilibrium in the full valence state of the compound [15].

Several techniques are used to obtain SnO_2 films, but the various processes present technical constraints on depositing sufficiently homogeneous layers. It was noted that the physical properties of the thin films depend strongly on the method of elaboration and the experimental conditions. Among the deposition methods, we are interested in the spray pyrolysis technique. This technique has several advantages, such as the possibility of using high purity precursors, the ease of deposition on large surfaces and complex shaped substrates, and all this at low temperatures and low cost [16]. The general principle of this technique is based on the vaporization and the projection of a solution of various reactive compounds, using an atomizer, on a heated substrate. The temperature of the substrate allows the activation of the chemical reaction between the compounds. The experiment can be carried out in air, and can be prepared in a chamber (or in a reaction chamber) under a vacuum reaction chamber with a vacuum of about 50 Torr. The description of the film formation by the spray pyrolysis method can be summarized as follows: (1) Formation of droplets at the nozzle outlet. (2) Decomposition of the precursor solution on the surface of the heated substrate by pyrolysis reaction [17]. In general, the systems used to produce a spray stream fall into two categories: Pneumatic spray (PSP) technique: in this case, it is the effect of the pressure of the carrier gas that causes the liquid to be sprayed in fine droplets. Ultrasonic spray technique: in this case, the atomization of the liquid is produced by ultrasonic waves. Several studies have been using pneumatic spray pyrolysis technique. Espindola-Rodriguez *et al*. [18] obtained high-quality Cu_2ZnSnS_4 thin films for photovoltaic applications. Also, Girtan *et al*. [17] prepared thin films of indium oxide by this techniques. On the other hand, cathodoluminescent and photoluminescent layers of terbium-doped ZrO_2 have been successfully synthesized by PSP deposition process [19].

The objective of this work is to improve the thermoelectric properties of the elaborate thin films based on undoped SnO_2 and doped with nickel (SnO_2/Ni at.%) for various content levels (2, 5 and 10 at.%) deposited on glass substrates at 450°C, by the pneumatic spray pyrolysis method. On the other hand, to study the influence of doping on the structural, optical and electrical properties of the films.

2. Experimental

2.1 *Films preparation*

The thin films of pure and nickel-doped tin oxide at 2 at.%, 5 at.%, and 10 at.% of Ni were prepared by pneumatic spray pyrolysis on a glass substrate, using tin chloride dehydrate content [$SnCl_2$-$2H_2O$] (purity: 99.99%) as a precursor, and nickel chloride [Ni] (purity: 90.00%) as a doping source.

The sputtering solution was prepared from a mixture of tin chloride [$SnCl_4$, $2H_2O$] (Fulka 99.9%) (0.6 g) dissolved in 10 ml of distilled water (resistivity = 18.2 MΩ cm) and 10 ml of methanol (CH_3OH) (Merck 99.5%) with a source of nickel ($NiCl_2$–$6H_2O$) (Fulka 99.9%) for different doping concentrations (2, 5 and 10 at.%). This solution was agitated for 1 h using a heated magnetic stirrer at room temperature. The thin films are deposited onto microscope coverglass substrates ($76.2\times25.4\times1.2$ mm^3) uheated at 450°C, with a flow rate of 20 ml h^{-1} and a pressure of 1.5 atm with a distance samples–nozzle of 25 cm during a 30 min deposition time.

2.2 *Characterization techniques*

After the elaboration of pure and nickel-doped tin oxide films (figure 1), it is necessary to carry out various characterizations, that allows to observe and optimize the influence of doping concentration.

The phase purity and crystallographic structure of the examined films were investigated using X-ray diffraction (XRD; PANalytical Empyrean diffractometer) at room temperature and Cu-Kα1 radiation (λ = 1.54056 Å) in the 2θ range 20–80°. We studied the surface morphology of the obtained films using a scanning electron microscope (SEM, a JEOL JSM 7500F microscope) equipped with energy dispersive X-ray spectroscopy (EDAX) to determine the elemental composition of the films. By means of a Thermo-Nicolet instrument, Fourier transform infrared (FTIR) spectra were recorded in the 4000–400 cm^{-1} region. The transmission spectra (T%) for optical properties were measured using a Perkin Elmer UV-VIS-NIR Lambda 19

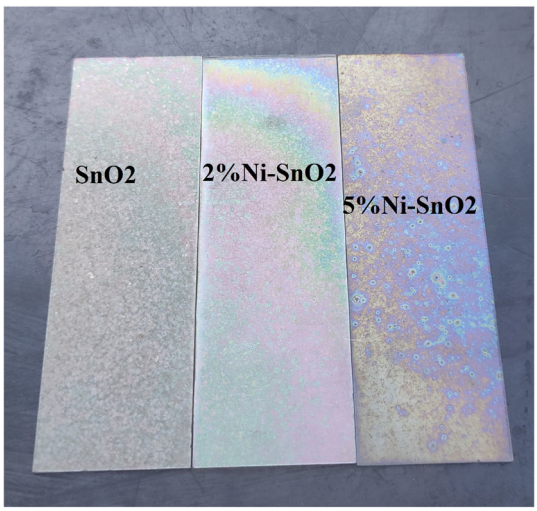

Figure 1. Digital images of SnO_2, 2%Ni–SnO_2 and 5%Ni–SnO_2 thin films.

spectrophotometer in the 190–1800 nm spectral range. Concerning the electrical properties, the standard four-point probe method was used. The Seebeck coefficient was established based on the detected Seebeck voltage and the gradient temperature from 0 to 200 K with an interval of 20 K.

3. Results and discussion

3.1 *Structural analysis*

The XRD spectra of SnO_2, $Sn_{1-x}Ni_xO_2$ [$0.00 < x \leq 0.10$] thin films, obtained by the pneumatic pyrolysis technique, is shown in figure 2. This shows that all the films crystallize into a rutile-like tetragonal structure of SnO_2 according to JCPDS card no: 77-0452, by the presence of peaks with directions (110), (101), (200), (211), (310) and (301) [20]. Moreover, the XRD spectra confirm the absence of any other diffraction peak related to metal clusters and/or oxide impurity phases such as NiO, NiO_2, which confirm the insertion of Ni into the SnO_2 lattice.

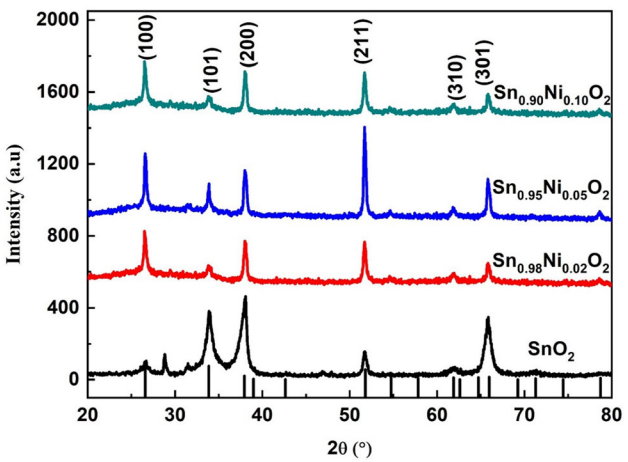

Figure 2. XRD patterns of Ni-doped SnO_2 sprayed thin films.

The intensity of the peaks varies with the doping content. It is also observed that the most intense peak (200) is located around the angle of 38.01° [21]. The intensity of peak (101) increases with the increase of Ni content, which indicates an improvement in the crystallinity of SnO_2, due to the similarity between the ionic radii of Sn^{4+} (69 Å) and Ni^{2+} (69 Å), which is preferable to Ni occupying the Sn sites [22]. In addition, a weak shift of the diffraction peaks towards smaller diffraction angles was observed with increasing Ni concentration. Therefore, Ni could expect alterations in the tetragonal structure of the SnO_2 host lattice due to the replacement of Sn, so we can conclude that the doping with nickel changes the structure of the elaborated films [23].

Moreover, the intensity of peaks (211) reaches its maximum intensity for a doping content of 5 at.%, and then decreases for a doping content of 10 at.%, which can be explained by the existence of the solubility limit of (Ni_{Sn}) into the SnO_2 matrix at $x = 0.05$ and the assembling between the two ionic radii of Sn^{4+} and Ni^{2+}.

The lattice parameters (a) and (c) of SnO_2 and Ni–SnO_2 thin films were obtained from the following formula [24]:

$$\frac{1}{d_{hkl}^2} = \frac{(h^2 + k^2)}{a^2} + \frac{l^2}{c^2} \quad (1)$$

where d_{hkl} is the inter-planar distance, (hkl) the indexes of Miller and the constants 'a' and 'c' of the lattice.

The Scherrer formula was used to determine the crystallite size (D) of these thin films [25,26].

$$D = \frac{k\lambda}{\beta\cos\theta} \quad (2)$$

In which D is the average crystallite size, k the Scherrer constant, here taken to be equal to 0.9, λ represents the X-ray wavelength (Cu Kα = 0.15406 nm), θ denotes the Bragg angle, and β expresses the total width of the diffraction line at half-maximum intensity (FWHM).

The results obtained are presented in table 1. The parameters of the lattice are found to increase as the Ni rate increases. It takes maximum values for a doping content of 2 at.% and then decreases to a doping content $\geq$5 at.%, but still remains higher than that of SnO_2. The rise of the lattice parameters with the increase of Ni could be explained by the incorporation of Ni ions into the SnO_2 matrix. On the other hand, a reduction in the FWHM with an increase in the intensity of the peaks suggests that the incorporation of Ni in the SnO_2 lattice leads to an increase in the grain size of the doped thin films. It can also be mentioned that the doping content (5 at.%) presents the solubility limit of (Ni_{Sn}) into SnO_2 matrix at $x = 0.05$ in our case, which is in agreement with other studies [16].

Table 1. Microstructural parameters of the studied $Sn_{1-x}Ni_xO_2$ thin films.

Sample	Plane*e* (*hkl*)	$2\theta_{hkl}$ (°)	$d_{spacing}$ (Å)	β (°)	Lattice constants (Å)		D (nm)	ε (%)	δ ($\times 10^9$ lines.mm^{-2})
					a	c			
SnO_2	(110)	26.61	3.349	3.542	4.7364	3.1830	27.62	0.443	1.410
	(101)	33.92	2.642	3.542					
	(200)	38.06	2.364	2.952					
	(211)	51.68	2.768	4.133					
$Sn_{0.98}Ni_{0.02}O_2$	(110)	26.52	3.359	1.467	4.7503	3.1825	45.86	0.373	0.475
	(101)	33.02	2.644	3.542					
	(200)	37.94	2.366	3.542					
	(211)	51.68	1.768	1.771					
$Sn_{0.95}Ni_{0.05}O_2$	(110)	26.54	3.357	1.771	4.7483	3.1893	47.28	0.320	0.447
	(101)	33.85	2.647	2.362					
	(200)	37.87	2.375	2.362					
	(211)	51.66	1.769	2.066					
$Sn_{0.90}Ni_{0.10}O_2$	(110)	26.54	3.358	2.362	4.7489	3.1935	32.25	0.328	0.961
	(101)	33.81	2.650	3.542					
	(200)	38.02	2.366	3.542					
	(211)	51.67	1.768	2.952					

The dislocation density (ε) and lattice strain (δ) were calculated using equations (3 and 4), respectively [27,28].

$$\varepsilon = \frac{\beta}{4\tan\theta} \tag{3}$$

$$\delta = \frac{1}{D^2} \tag{4}$$

The results of the strain (ε) and the dislocation density (δ) illustrated in table 1, increased with the increase of Ni concentration, confirm the amelioration of crystallinity.

3.2 *Surface morphology*

We performed microstructural studies of pure and nickel-doped SnO_2 thin films to highlight some effects due to the change in doping content. Scanning electron microscopy (SEM) micrographs of the surface of $Sn_{1-x}Ni_xO_2$ layers ($x = 0.02$, 0.05 and 0.10) are shown in figure 3a–d, respectively. The SEM observations showed that the Ni–SnO_2 layers have tightly packed regular grains with an almost smooth grain surface, fine and small grain size distribution, with no pin-holes and fissures.

3.3 *Compositional analysis*

Figure 4 shows the EDAX analysis of SnO_2, $Sn_{1-x}Ni_xO_2$ [$x = 0.02$, 0.05 and 0.10] films obtained by spray pyrolysis, revealing the presence of tin, nickel and oxygen in nearly stoichiometric amounts, which clearly shows the absence of any impurity elements in the obtained samples. The remaining peaks that appear in the EDAX spectra, except for those of Sn, Ni and O, are due to elements that compose the glass substrate, such as Si, Mg and P [13].

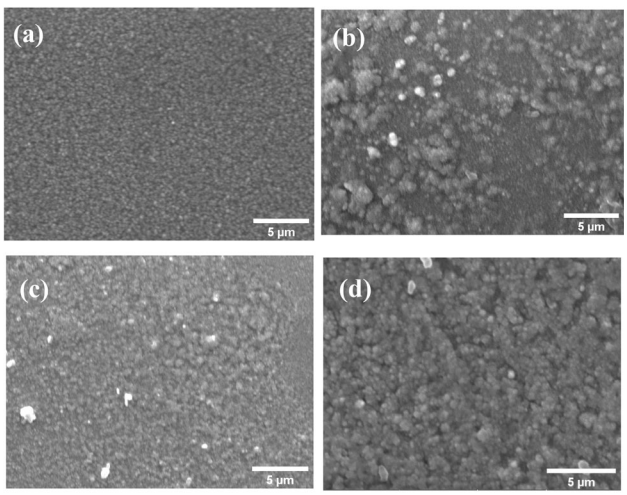

Figure 3. SEM images of nickel-doped SnO_2 sprayed thin layers: (**a**) 0 at.%, (**b**) 2 at.%, (**c**) 5 at.% and (**d**) 10 at.%.

Consider that the films are stoichiometric of the form $Sn_{1-x}Ni_xO_2$ [$x = 0.02$, 0.05 and 0.10]. Here the stoichiometric of the films is found from the Ni and Sn signals only. From the relation equation (5) [29].

$$x = r/r + 1 \tag{5}$$

In this study, x is the atomic Ni content and r is the ratio of Sn to Ni EDAX signals (table 2). Figure 5 represents the relationship between the Ni and Sn EDAX signals and the estimated value of the Ni atomic content both plotted against the 'expected' Ni content of the deposit. It can seem

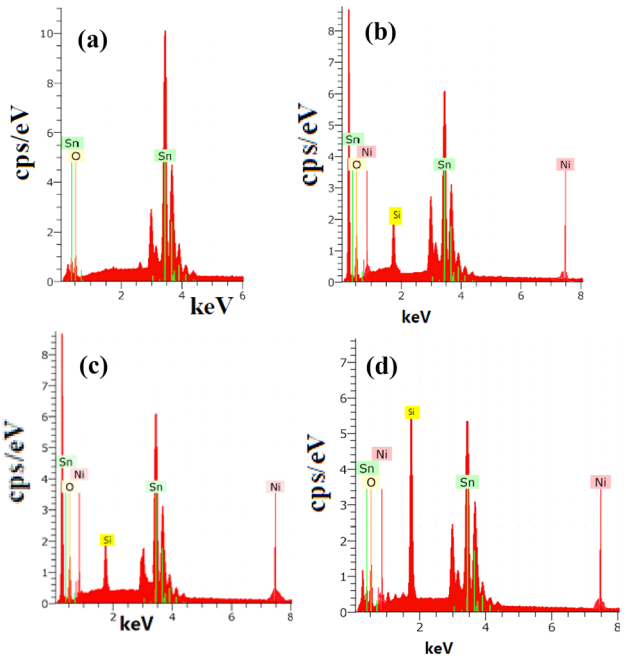

Figure 4. EDAX elemental composition analysis of (**a**) SnO_2, (**b**) SnO:Ni 2 at.%, (**c**) SnO_2:Ni 5 at.% and (**d**) SnO_2:Ni 10 at.% thin films.

that the incorporation of Ni into the lattice is very evident for all dopant levels.

3.4 *FT-IR spectroscopy*

Figure 6 shows the FT-IR spectra of the prepared pure and Ni-doped SnO_2 film by spray pyrolysis. The presence of a band around 633 cm^{-1}may be associated with the vibration of Sn–O and Ni–O bonding [30–32]. However, this band is shifted with the doping concentration, and in addition, the intensity of this band is decreased and almost disappears for a doping content of 10 at.%. That confirms the substitution of Ni in the host lattice of SnO_2. It is also noticed that the FT-IR spectrum of the $Sn_{0.95}Ni_{0.05}O_2$ sample is well defined due to the crystallinity improvement, confirming that 5 at.% doping presents the existence of the solubility limit of (Ni_{Sn}) into the SnO_2 matrix at $x > 0.05$ in our case. In addition, there is a peak located around 1640 cm^{-1}, corresponding to the bending vibration O–H oscillators in the adsorbed water molecules and in the alcohol, respectively, while another band at 3444 cm^{-1} can be attributed to the stretching vibration O–H [29].

3.5 *Optical properties*

Figure 7 shows the variation of the transmittance as a function of the wavelength in the range [190–1100 nm] for the undoped and Ni-doped SnO_2 samples prepared at different contents (2, 5 and 10 at.%). It can seem that all the layers show good optical transparency in the visible range, with a transmission value that varies between 76 and 82% in the visible range after doping. This result shows that Ni doping improves the optical properties that have an important role in photovoltaic devices [33,34]. It is also noted that the 10 at.% Ni-doped layer has the highest transparency in the visible range.

In addition, the transmission edge shifts to lower wavelengths (blue shift) with the doping, resulting in an increase in the bandgap energy.

Based on the model of Wemple [35–38], relying on the study of a single oscillator, it is possible to determine the different dispersion parameters of our Ni-doped SnO_2 thin films. In figure 7, the continuous line represents the fitting curve and the symbols are the experimental data. The values obtained are listed in table 3.

An increase in the optical bandgap energy is noticed at values of 3.83, 3.98, 3.99 and 4.01 eV for the SnO_2, $Sn_{0.98}Ni_{0.02}O_2$, $Sn_{0.95}Ni_{0.05}O_2$ and $Sn_{0.90}Ni_{0.10}O_2$ thin films, respectively. This increase can be explained by the distortions caused in the crystallographic lattice of SnO_2. It can also be found that the introduction of more Ni gives an increase in the optical bandgap energy. This increase is often reported in the literature and is referred to as the Burstein-Moss effect [39]. This can be due to the increase in the number of charge carriers (electrons) from the donor Ni^{2+} ions that are incorporated into the substitutional or interstitial locations of the Sn^{4+} cation. This rise in the optical bandgap energy values confirms the incorporation of Ni^{2+} ions into the SnO_2 host lattice, which is in agreement with the XRD results.

The calculated refractive index spectra (n) [40,41] for the elaborated $Sn_{1-x}Ni_xO_2$ layers are presented in figure 8. The

Table 2. Composition and stoichiometry of the SnO_2, $Sn_{1-x}Ni_xO_2$ [$x = 0.00$, 0.02, 0.05 and 0.10] thin films obtained by statistical analysis of EDS spectra.

$Sn_{1-x}Ni_xO_2$ [$x = 0.00$, 0.02, 0.05 and 0.10] 'Nominal' Ni content (at.%)	Sn (at.%)	O (at.%)	Ni (at.%)	x (Ni) 'EDS' Ni content (at.%)
SnO_2	82.68	17.32	—	—
$Sn_{0.98}Ni_{0.02}O_2$	62.40	36.03	1.57	0.0244
$Sn_{0.95}Ni_{0.05}O_2$	72.52	23.40	4.08	0.0532
$Sn_{0.90}Ni_{0.10}O_2$	63.41	30.01	6.49	0.1012

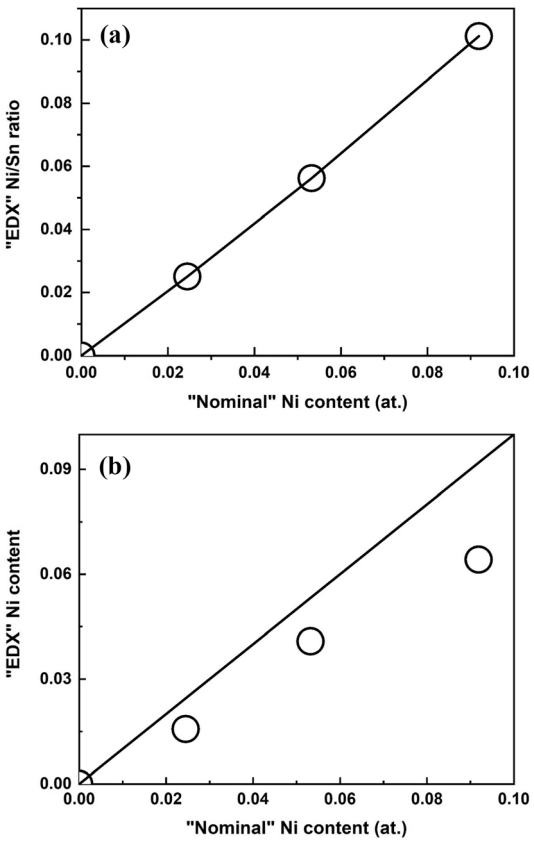

Figure 5. (**a**) Ni/Sn atomic ratio and (**b**) Ni atomic content (measured with EDAX) plotted as a function of the expected Ni content.

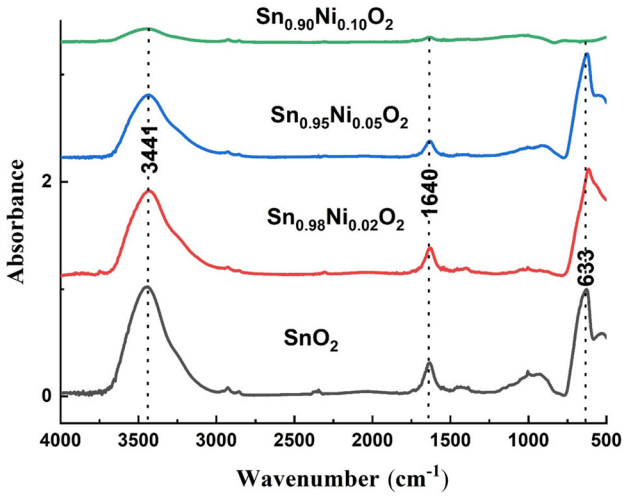

Figure 6. FT-IR spectra of the SnO_2, $Sn_{0.95}Ni_{0.05}O_2$ [$x = 0.02$, 0.05 and 0.10] samples.

refractive index values decrease with a further increase in Ni content. This decrease in refractive index can be attributed to the existence of defects and impurities in the thin films resulting from Ni doping.

The calculated thicknesses (d) [40,41] of Ni-doped SnO_2 thin films obtained by spray pyrolysis are reported in table 3. It is our understanding that, in fact, the thickest thin films diffuse a minimal amount of light. This is evident in all our results, for example, the thin films doped at $x = 10$ at.% have the minimum value of thickness and the highest value of transmittance.

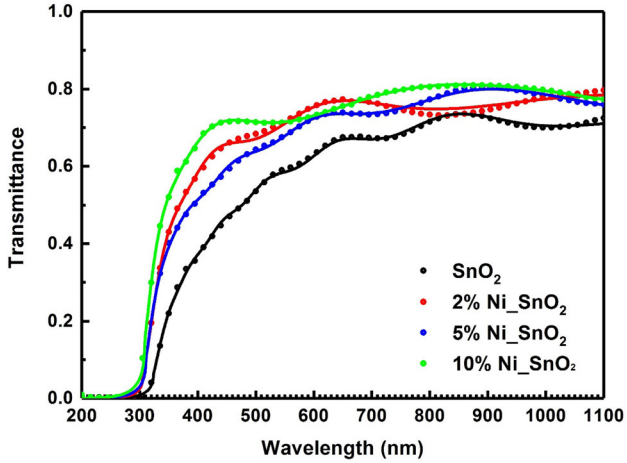

Figure 7. Transmission spectra of SnO_2, $Sn_{0.95}Ni_{0.05}O_2$ [$x = 0.02$, 0.05 and 0.10]. Measured (full circles) and calculated (solid lines) transmittance spectra of films.

Table 3. Dispersion parameters of the SnO_2, Ni–SnO_2 films extracted by fitting the experimental data.

Samples	Thickness (nm)	E_g (eV)	n at 598 nm	n_∞
SnO_2	712	3.83	1.80	1.74
2% Ni–SnO_2	349	3.98	1.74	1.75
5% Ni–SnO_2	520	3.99	1.79	1.70
10% Ni–SnO_2	234	4.01	1.79	1.74

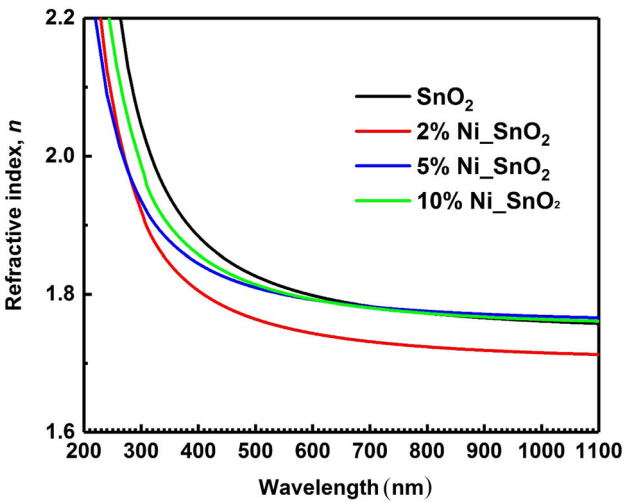

Figure 8. Refractive index of SnO_2, $Sn_{0.95}Ni_{0.05}O_2$ [$x = 0.02$, 0.05 and 0.10] films.

3.6 *Electrical properties*

The electrical properties of SnO_2 thin films are of considerable interest, especially with respect to the applications envisaged in the optoelectrical field. We recall that our main objective is to improve and optimize the electrical conductivity (σ) of the films while maintaining high optical transparency with doping [42,43]. The effect of nickel doping on the resistivity (ρ) of SnO_2:Ni films are presented in table 4. To further test the homogeneity of our samples, the electrical sheet resistance (R_{sheet}), average optical transmittance at 550 nm wavelength, and merit figure (ϕ_{TC}) are presented in table 4. From these results, the increase in sheet resistance with the increase in Ni content is due to the impurity scattering effect of Ni.

The FOM (ϕTC) is a valuable means to evaluate the performance of transparent conductive films with different resistivity and transparency, was calculated utilizing the following equation (6) [44],

$$\phi_{TC} = T^{10}/R_{sheet} \quad (6)$$

where T is the optical transmittance (at 550 nm), and R_{sheet} is the sheet resistance. The highest FOM was obtained for 2%Ni–SnO_2 films at 349-nm thick sample due to its high transmittance (0.716) and low sheet resistance (380 Ω sq^{-1}). The lowest FOM was observed for undoped SnO_2 films at 712 nm. It was caused mainly because of very low transmittance (0.596). We found that the smallest FOM was obtained for the thinnest film in our study for undoped SnO_2 films, which indicates that doping with Ni ameliorates the transmittance value and the thinnest. In the present study, this Φ value is smaller than that reported in the literature for FTO thin films synthesized by the spray pyrolysis method, such as SnO_2:In (ITO) 6.4 $\times$ 10^{-3} Ω^{-1} [45]; SnO_2:Ti 5 $\times$ 10^{-3} Ω^{-1} [46]; ZnO:Al (AZO) 1.518 $\times$ 10^{-3} Ω^{-1} [47]; ZnO:Ga (GZO) 4.57 $\times$ 10^{-3} Ω^{-1} [48]; ZnO:Si 4.15 $\times$ 10^{-3} Ω^{-1} [49]; ZnO:Al and In(AIZO) 4.09 $\times$ 10^{-3} Ω^{-1} [50]; TiO_2 3.8 $\times 10^{-3}$ Ω^{-1} [51] and $BaSnO_3$:La 5 $\times$ 10^{-3} Ω^{-1} [52].

The resistivity (ρ) and conductivity (σ) values of the films are grouped in table 4. It is noticed that the conductivity increases by 64, 75, 32 and 40 Ω cm^{-1}, while the resistivity decreases by 1.56, 1.32, 3.12 and 2.50×10^{-2} Ω cm, with the content of doping (0, 2, 5 and 10 at.%), respectively. In other words, the decrease in resistivity (increase in conductivity) as a function of doping content is probably due to the decrease in thickness of the thin films prepared.

The lowest resistivity was found in the case of the 2 at.% Ni film (ρ_{min} = 0.0132 Ω cm). This decrease in resistivity is possibly due to the replacement of the Sn^{4+} cation by cations from doping (Ni^{2+} ion) in substitutional or interstitial locations. The presence of a small percentage of Ni^{2+} ions relative to Sn^{4+} ions is desirable to accentuate the decrease in resistivity.

Such behaviour can be interpreted by the increase of defects, introducing the formation of intermediate states in the bandgap [53,54]. This result is in very good agreement with the optical properties, more precisely with the interpretation proposed in the decrease of transmittance, have interpreted a similar decrease in SnO_2 thin films doped with Ni with the increase in crystallite size and, consequently, a reduction in the size of grain boundaries. From the results, it is also noticed that there is an increase in resistivity at 5 at.% Ni content. It can be assumed that an increase in electrical resistivity is attributed to the decrease in charge carrier mobility.

3.7 *Seebeck coefficient*

The evolution of the Seebeck coefficient |S| at gradient temperatures (0 to 200 K) is shown in figure 9. All these samples have a negative Seebeck coefficient, which confirms that they are n-type semiconductors [55].

The insertion of Ni into the SnO_2 mesh leads to a change in the Seebeck coefficient of the samples. The Seebeck coefficient of the samples $x = 0.02$ and $x = 0.10$ is decreased in comparison with that of the undoped SnO_2

Table 4. Electrical properties of the SnO_2, $Sn_{1-x}Ni_xO_2$ [x = 0.00, 0.02, 0.05 and 0.10] films.

Samples	Resistance (R_{sheet}) Ω sq^{-1}	Average transmittance at 550 nm	Merit of figure, (ϕ) Ω^{-1}	Resistivity, (ρ) ($\times10^{-2}$), Ω cm	Conductivity (σ) Ω^{-1} cm^{-1}
SnO_2	220	0.596	2.57×10^{-5}	1.56	64
2%Ni–SnO_2	380	0.716	9.31×10^{-5}	1.32	75
5%Ni–SnO_2	600	0.682	3.62×10^{-5}	3.12	32
10%Ni–SnO_2	500	0.713	6.79×10^{-5}	2.50	40

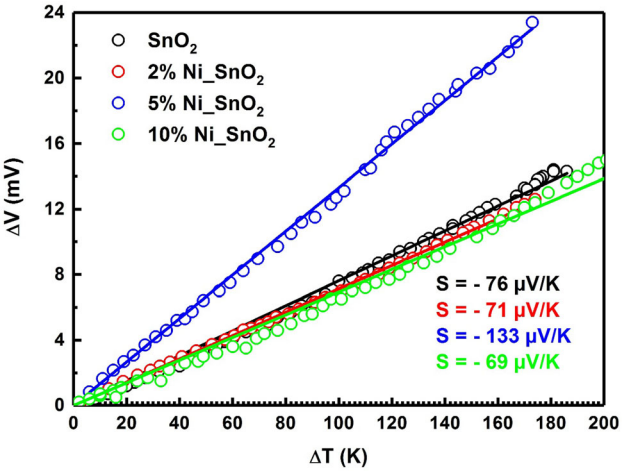

Figure 9. Seebeck coefficients for SnO_2, $Sn_{0.95}Ni_{0.05}O_2$ [$x = 0.02$, 0.05 and 0.10] thin films.

sample. The Seebeck coefficient decreases as a function of the Ni content; nevertheless, this variation is not very significant. This result is in agreement with the result reported by Yanagiya *et al*. [56]. However, for a doping content of 10 at.%, the Seebeck coefficient is nearly twice as large as that of pure SnO_2.

The Seebeck coefficient decreases as a function of the doping concentration, i.e., with the increase of charge carriers. For $x = 0.02$ and 0.10, the evolution of the Seebeck coefficient as a function of the Ni content is difficult to interpret directly. As previously stated, since the solubility limit is about $x = 0.05$, a phase with high electrical resistivity (3.12×10^{-2} Ω cm), can be formed at the joints of doped SnO_2 grains once $x = 0.05$. This impurity may be the cause of the increase in the Seebeck coefficient for $x = 0.05$ doped samples.

The carrier concentration can be obtained from the following equations [57]: when $|S| > 75$ µV K^{-1}

$$m_S^* = \frac{h^2}{2k_BT}\left\{\frac{3n}{16\sqrt{\pi}}\left(\exp\left[\frac{|S|}{(k_B/e)}-2\right]-0.17\right)\right\}^{2/3} \quad (7)$$

and, when $|S| > 75$ µV K^{-1}

$$m_S^* = \frac{3h^2}{8\pi^2k_BT}\frac{|S|}{(k_B/e)}\left(\frac{3n_H}{\pi}\right)^{2/3} \quad (8)$$

where e is the charge of the carriers, k_B the Boltzmann constant, T represents the absolute temperature, h corresponds to the Planck constant, and $m_S{}^*(m_S{}^* = 0.216m_0)$ indicates the effective return mass of SnO_2 and n the carrier concentration. According to table 5, the increase in carrier concentration should result in both an increase in σ and a decrease in |S|. In this study, the carrier concentration increases for the entire sample, on the contrary to the conductivity, which is sensitive to the change in thickness.

Table 5. Seebeck coefficients values of the SnO_2, $Sn_{1-x}Ni_xO_2$ [$x = 0.00$, 0.02, 0.05 and 0.10] films.

Samples	S, µV K^{-1}	n, cm^{-3}	E_F, meV
SnO_2	−76	1.96×10^{19}	96
2% Ni–SnO_2	−71	6.17×10^{19}	103
5% Ni–SnO_2	−133	6.66×10^{18}	55
10% Ni–SnO_2	−69	6.44×10^{19}	106

Ni could relate the increase in n to the substitution of Sn, because it can be assumed that the substitution increases the value of n because Ni is divalent and Sn is quadrivalent, which results in the presence of additional electrons.

The degenerate character of our SnO_2, $Sn_{1-x}Ni_xO_2$ [$x = 0.02$, 0.05 and 0.10] thin films is verified by determining the Fermi energy level (E_F) by utilizing the following relationship [58]:

$$E_F = \frac{\pi^2k_B^2T}{3|e||S|} \quad (9)$$

The Fermi energy calculation is between 55 and 106 meV (figure 10). We notice that the Fermi energy level (E_F) increases with Ni doping. This confirms the substitution of the Sn^{4+} ion by the Ni^{2+} ion in the SnO_2 lattice. These electrons occupy states in the conduction band, causing a movement from the Fermi level to higher energy in the conduction band. Furthermore, since all states below the Fermi level are occupied states, the electron can only be excited from the top of the valence band to the conduction band above the Fermi level. The exclusion principle of Pauli avoids the excitation of these occupied states. Therefore, an increase in the bandgap energy was detected. Due to this, the observed blue shift indicates an unimportant improvement in the band structure of Ni-doped SnO_2 films

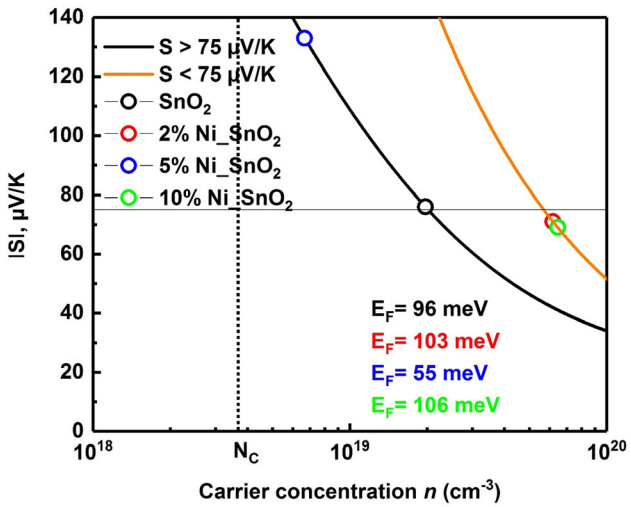

Figure 10. Seebeck coefficients as a function of carrier concentrations for SnO_2, $Sn_{0.95}Ni_{0.05}O_2$ [$x = 0.02$, 0.05 and 0.10] thin films.

due to the incorporation of Ni^{2+} ions. For the reduction of the E_F value for 5 at.% Ni–SnO_2 thin films, this confirms the existence of the solubility limit of (Ni_{Sn}) into the SnO_2 matrix at $x = 0.05$.

These conclusions can be reinforced by calculating the values of the effective density (N_c) in the conduction band and applying the relation [59], which enables interpolation of the interval between non-degenerate and degenerate semiconductors.

$$Nc = 2\left(\frac{2\pi m_S^* k_B T}{h^2}\right)^{3/2} \quad (10)$$

We obtain a value for the effective density of SnO_2 that is 3.63×10^{18} cm^{-3}. Figure 9 displays the degeneracy of SnO_2, $Sn_{1-x}Ni_xO_2$ [$x = 0.02$, 0.05 and 0.10] thin films.

We noted that the thin films of $Sn_{0.98}Ni_{0.02}O_2$ and $Sn_{0.90}Ni_{0.10}O_2$ are highly degenerated except for $Sn_{0.95}Ni_{0.05}O_2$, which indicates that this element promotes electron formation, which confirms the substitution of ions in the SnO_2 host lattice. However, in the case of doping with the elements cobalt and nickel the product is less degenerated than SnO_2, which indicates that these elements do not promote electron formation, which confirms that these elements entered the SnO_2 lattice as impurities. We find that the thin films of $Sn_{0.98}Ni_{0.02}O_2$ and $Sn_{0.90}Ni_{0.10}O_2$ are highly degenerated, suggesting that this concentration favours electron formation. However, for the thin films of $Sn_{0.95}Ni_{0.05}O_2$ that are less degenerated, they can be interpreted in this way: At a low doping content, the introduction of nickel can be in the form of impurities in the interstitial sites, creating a disorder in the SnO_2 lattice. In addition, at a doping content of ($x = 0.05$) the Ni^{2+} ions will occupy all the sites that make the lattice more stable, whereas at a doping content of ($x = 10$ at.%), the layers will be strongly degenerated due to the excess of electrons and thus more movement resulting in the disorder.

This confirms two points: one is that Ni^{2+} ions are substituted in the lattice and the second is that the existence of solubility limits (5 at.%) doping content. In addition, the thermoelectrical study is more sensitive to the defects in the nanomaterials and provides findings that cannot be indicated by the XRD.

4. Conclusion

This study consisted of the elaboration and characterization of SnO_2, $Sn_{1-x}Ni_xO_2$ [$x = 2$, 5 and 10 at.%] thin films deposited by the pneumatic spray pyrolysis technique in order to study the influence of nickel doping on the different structural, microstructural, optical and electrical properties of the films obtained. The results of the XRD characterization show that all the films are polycrystalline with a tetragonal structure of the rutile type. The increase in the concentration of the Ni dopant clearly causes an increase in the intensity of the peaks. All the Ni-doped SnO_2 films showed a preferential growth trend along the (200) direction. The average crystallite size varied between 27 and 47 nm. SEM revealed a smooth surface. The FT-IR analysis shows an increase in the Sn–O peak intensities for the 2 at.% Ni and 5 at.% Ni films, but this peak changes squarely for a 10 at.% doping content. The UV–visible spectrophotometer analysis represents an important feature in evaluating the quality of the deposited films. The average transmittance was found to be around 76–82% with the presence of an interference fringe.

In the visible range, which indicates that our films are homogeneous and smooth, in other words, the values of optical bandgap energy obtained from our films are in the range of 3.83–4.01 eV. The refractive index values are strongly related to the optical bandgap energy. The electrical characteristics of the films show that the resistivity increases as the concentration of Ni dopants in the solution increase, moreover, the minimum resistivity of 1.32×10^{-2} Ω cm is obtained for the 2 at.% Ni-doped SnO_2 thin films. Performance of Ni–SnO_2 thin films was compared for each thickness using FOM. This investigation has shown that 2%Ni–SnO_2 thin film with thickness of 349 nm has the highest transmittance and simultaneously the highest FOM. The Seebeck coefficient values varied as a function of doping concentration. This result is interpreted by the increase in the number of charge carriers (electrons) from Ni^{2+} donor ions incorporated into the substitutional or interstitial locations of Sn^{4+} cations.

References

[1] Roguai S and Djelloul A 2022 *ALJEST* **8** 2285
[2] Yates Heather M, Evans P, Sheel David W, Nicolay S, Ding L and Ballif Ch 2012 *Surf. Coat. Technol.* **213** 167
[3] Zebbar N, Aida M S, Hafdallah A E K, Daranfad O, Lekiket H and Kechouane M 2009 *Mater. Sci. Forum.* **609** 133
[4] Indrajit M, Kiruthika S, Ganesha Mukhesh K, Baral M, Kumar A, Vimala S *et al* 2021 *J. Mater. Chem. A* **9** 23157
[5] Bilgin V, Akyuz I, Ketenci E, Kose S and Atay F 2010 *Appl. Surf. Sci.* **256** 6586
[6] Miao D, Zhao Q, Wu S, Wang Z, Zhang X and Zhao X 2010 *J. Non-Cryst. Solids* **356** 2557
[7] Zhao Li D, Chang C, Tan G and Kanatzidis M G 2016 *Energy Environ. Sci.* **9** 3044
[8] Luo Y, Zheng Y, Luo Z, Hao S, Du C, Liang Q *et al* 2017 *Adv. Energy Mater.* **1702167** 1
[9] Tan G, Shi F, Hao S, Chi H, Bailey T P, Zhao L D *et al* 2015 *J. Am. Chem. Soc.* **137** 1150
[10] Banyamin Z Y, Kelly P J, West G and Boardman J 2014 *Coatings* **4** 732
[11] Soitah T N, Yang C and Sun L 2010 *Mat. Sci. Semicon. Proc.* **13** 125
[12] Li Y, Yin W, Deng R, Chen R, Chen J, Yan Q *et al* 2012 *NPG Asia Mater.* **4** e30

[13] Roguai S and Djelloul A 2022 *Inorg. Chem. Commun.* **138** 109308
[14] Roguai S and Djelloul A 2022 *Solid State Commun.* **350** 114740
[15] Li Y, Zhou W, Wang J, Yang Y and Wu P 2017 *Mater. Chem. Phys.* **199** 216
[16] Amer M I, Moustafa S H and El-Hagary M 2020 *Mater. Chem. Phys.* **248** 122892
[17] Girtan M, Cachet H and Rusu G I 2003 *Thin Solid Films* **427** 406
[18] Espindola-Rodriguez M, Placidi M, Vigil-Galán O, Izquierdo-Roca V, Fontané X, Fairbrother A *et al* 2013 *Thin Solid Films* **535** 67
[19] Garcı´a-Hipo´litoa M, Martı´neza R, Alvarez-Fregosoa O, Martı´neza E and Falcony C 2001 *J. Lumin.* **93** 9
[20] Daranfed W, Aida M S, Attaf N, Bougdira J and Rinnert H 2012 *J. Alloys Compd.* **542** 22
[21] Houaidji N, Ajili M, Chouial B and Turki Kamoun 2020 *Optik* **208** 164026
[22] Henry J, Mohanraj K, Sivakumar G and Umamaheswari S 2015 *Acta Part A Mol. Biomol. Spectr.* **143** 172
[23] Ahmed A, Ali T, Naseem Siddique M, Ahmad A and Tripathi P 2017 *J. Appl. Phys.* **122** 083906
[24] Benhaoua A, Rahal A, Benhaoua B and Jalaci M 2014 *Superlattice Microst.* **70** 61
[25] Abdelkrim A, Rahmane S, Abdelouahab O, Abdelmalek N and Brahim G 2016 *Optik* **127** 2653
[26] Bagheri-Mohagheghi M M, Shahtahmasebi N, Alinejada M R, Youssefi A and Shokooh- Saremi M 2009 *Solid State Sci.* **11** 233
[27] Williamson G K and Smallman R E 1956 *Philos. Mag.* **1** 34
[28] Mariappan R, Ponnuswamy V, Ragavendar M, Krishnamoorthi D and Sankar C 2012 *Optik-Int. J. Light Electron. Opt.* **123** 1098
[29] Roguai S and Djelloul A 2021 *Solid State Commun.* **334** 114362
[30] Fujihara S, Maeda T, Ohgi H, Hosono E, Imai H and Sae-Hoon Kim 2004 *Langmuir* **20** 6476
[31] Liu Y, Yang F and Yang X 2008 *Colloids Surf. A* **312** 219
[32] Mu J, Chen B, Guo Z, Zhang M, Zhang Z, Shao C *et al* 2011 Colloid. *Interface Sci.* **356** 706
[33] Ajili M, Castagné M and Kamoun Turki N 2015 *Optik* **126** 708
[34] Ajili M, Castagné M and Kamoun Turki N 2014 *J. Lumin.* **150** 1
[35] Roguai S and Djelloul A 2019 *Appl. Phys. A* **125** 816
[36] Roguai S and Djelloul A 2020 *Appl. Phys. A* **126** 122
[37] Segnit E R and Holland A E 1965 *Ceram. Soc.* **48** 412
[38] Xin M 2019 *Surf. Eng.* **35** 947
[39] Burstein E 1954 *Phys. Rev.* **93** 632
[40] Roguai S, Djelloul A, Nouveau C, Souier T, Dakhel A A and Bououdina M 2014 *J. Alloys Compd.* **599** 150
[41] Roguai S and Djelloul A 2021 *React. Kinet. Mech. Catal.* **132** 1225
[42] Chatelon J P, Terrier C and Roger J A 1999 *Semicond. Sci. Technol.* **14** 642
[43] Edson R, Leite M and Inset B 2004 *Thin Solid Films* **449** 67
[44] Haacke G 1976 *J. Appl. Phys.* **47** 4086
[45] Kaleemulla S, Reddy A S, Uthanna S and Reddy P S 2009 *J. Alloys Compd.* **479** 589
[46] Khelifi C and Attaf A 2020 *Surf. Interfaces* **18** 100449
[47] Kalvani P R, Jahangiri A, Shapouri S, Sari A and Jalili Y S 2019 *Superlattice Microst.* **132** 106173
[48] Chaabouni F, Khalfallah B and Abaab M 2016 *Thin Solid Films* **617** 95
[49] Das D and Karmakar L 2020 *J. Alloys Compd.* **824** 153902
[50] Jayaraman V K, Alvarez A M, Bizarro M, Koudriavtsev Y and Amador M L O 2017 *Thin Solid Films* **642** 14
[51] Singh S, Sharma V, Saini D and Sachdev K 2017 *AIP Conf. Proc.* **1832** 080008
[52] Gogova D, Suwardi A, Kuznetsova Y A, Zatsepin A F, Mochalov L A, Nezhdanov A *et al* 2017 *Int. J. Adv. Appl. Phys. Res.* **4** 1
[53] Elangovan E and Ramamurthi K 2003 *J. Optoelectron. Adv. Mater.* **5** 45
[54] Agashe C and Major S S 1996 *J. Mater. Sci.* **31** 2965
[55] Tsubota T, Kobayashi S, Murakmi N and Ohno T 2014 *J. Electron. Mater.* **43** 3567
[56] Yanagiya S, Nong NV, Xu J and Pryds N 2010 *Materials* **3(1)** 318
[57] Zevalkink A, Smiadak D M, Blackburn J L, Ferguson A J, Chabinyc M L, Delaire O *et al* 2018 *Appl. Phys. Rev.* **5** 021303
[58] MacDonald D K C 1962 *Thermoelectricity: an introduction to the principles* (New York, London: Wiley)
[59] Boy J, Handwerg M, Ahrling R, Mitdank R, Wagner G, Galazka Z *et al* 2019 *APL Mater.* **7** 022526